SOLAR LIMB PROMINENCE CATCHER AND TRACKER (SLIPCAT): AN AUTOMATED SYSTEM AND ITS PRELIMINARY STATISTICAL RESULTS

Yuming Wang[1], Hao Cao[1], Junhong Chen[1], Tengfei Zhang[1], Sijie Yu[1], Huinan Zheng[1], Chenglong Shen[1],
Jie Zhang[2], and S. Wang[1]

[1] Key Laboratory of Basic Plasma Physics of CAS, School of Earth & Space Sciences, University of Science & Technology of China, Hefei, Anhui 230026, China;
ymwang@ustc.edu.cn

[2] Department of Computational and Data Sciences, George Mason University, 4400 University Dr., Fairfax, VA 22030, USA

ABSTRACT

In this paper, we present an automated system, which has the capability to catch and track solar limb prominences based on observations from the extreme-ultraviolet (EUV) 304 Å passband. The characteristic parameters and their evolution, including height, position angle, area, length, and brightness, are obtained without manual interventions. By applying the system to the *STEREO-B*/SECCHI/EUVI 304 Å data during 2007 April–2009 October, we obtain a total of 9477 well-tracked prominences and a catalog of these events available online. A detailed analysis of these prominences suggests that the system has a rather good performance. We have obtained several interesting statistical results based on the catalog. Most prominences appear below the latitude of $60°$ and at the height of about 26 Mm above the solar surface. Most of them are quite stable during the period they are tracked. Nevertheless, some prominences have an upward speed of more than 100 km s^{-1}, and some others show significant downward and/or azimuthal speeds. There are strong correlations among the brightness, area, and height. The expansion of a prominence is probably one major cause of its fading during the rising or erupting process.

Key words: catalogs – Sun: filaments, prominences – techniques: image processing

Online-only material: color figures

1. INTRODUCTION

Solar prominences, also called filaments when they are viewed on-disk, are long observed but still not well-known structures in the solar atmosphere. Since they are outstanding features in multiple-wavelength observations of the Sun and have close relationships with various solar eruptive phenomena, prominences are always one of the major topics in solar and space physics. The key issues in prominence/filament studies are their formation, maintenance, dynamic processes, and their roles in other related solar activities, e.g., coronal mass ejections (CMEs) and flares. With the aid of modern sensor technology, many facts of prominences are revealed (e.g., Poland 1986; Tandberg-Hanssen 1995; Martin 1998; Patsourakos & Vial 2002, and references therein). Prominences are dense (electron density $\sim 10^9$–10^{11} cm^{-3}) and cool ($\sim$5000–8000 K) plasmas floating in hot and diluted solar corona (e.g., Engvold & Brynildsen 1986; Hiei et al. 1986; Hirayama 1986; Madjarska et al. 1999). They can appear in any location from active regions to polar regions, and live for days to months. They have spines and barbs, and always straddle above polarity inversion lines. There are sometimes strong counterstreamings along spines and very dynamic vertical flows. The chirality of prominences/filaments obeys the pattern that most prominences on northern hemisphere are dextral while most ones on southern hemisphere are sinistral. The association rate of eruptive prominences with CMEs is more than about 70% (e.g., Gilbert et al. 2000; Gopalswamy et al. 2003).

Many of the above findings are made through statistical investigations combined with case studies. A continuously updated catalog of prominences with unbiased parameters is undoubtedly helpful for such researches, especially in the age of the explosive growth of observational data. For instance, the successful launch of the *STEREO* spacecraft (A and B) in 2006

led to the amount of solar observations explosively growing to more than 12 GB a day, and now it has increased to about 2 TB a day from the *Solar Dynamic Observatory* (*SDO*), which was just launched in 2010 February. NOAA/SWPC[3] routinely compiles a list of solar events in which on-disk filaments and limb-eruptive prominences are included; but the list is far from complete. Thanks to the unique properties of prominences/filaments, they can be clearly observed at multiple wavelengths, such as Hα, He I 10830 Å, He I 304 Å, radio waves, etc. (e.g., Schmahl et al. 1974; Hanaoka et al. 1994; Penn et al. 1994; Chiuderi Drago et al. 2001; Labrosse & Gouttebroze 2001), and therefore it is possible to extract them from the vast amount of data automatically and consistently.

Recognitions of on-disk filaments and limb prominences are different. The former is mainly accomplished by studying Hα data. For example, Gao et al. (2002), Shih & Kowalski (2003), Fuller et al. (2005), and Zharkova et al. (2005) developed codes to automatically detect filaments in full-disk Hα images. The automated system developed by Bernasconi et al. (2005) is able to detect, classify, and track Hα filaments efficiently. Extreme-ultraviolet (EUV) observations are much more difficult to use in detecting on-disk filaments due to the low contrast of filaments and the involvement of coronal holes. However, EUV observations are suitable for limb prominence detection. Through the usage of Fe IX/X 171 Å, Fe XII 195 Å, Fe XV 284 Å, and He II 304 Å images from the *Solar and Heliospheric Observatory* (*SOHO*)/EIT (Delaboudiniere et al. 1995) instrument, Foullon & Verwichte (2006) developed algorithms to recognize limb prominences. In their method, He II 304 Å data provide the basic criteria for the selection of candidate prominence regions, and other emission lines are used to remove active regions, which also appear brightly in EUV 304 Å. Most recently, Labrosse

---
[3] http://www.swpc.noaa.gov/Data/index.html

et al. (2010) also developed an efficient code to detect limb prominences in EUV 304 Å images.

In this paper, we present an automated system of detecting and tracking solar limb prominences based on only He II 304 Å data, and a resultant online catalog as well, which can be continuously updated. The performance and limitations of the system are presented in Section 3. Based on our catalog, some preliminary statistical results of solar limb prominences are also presented. The reasons why we choose the He II 304 Å emission line rather than Hα are the following. First, for prominence/filament observations, the He II 304 Å line is the only one uninterruptedly imaging the Sun with high cadence (operated by space-borne instruments SECCHI/EUVI on board the *STEREO* twins, and AIA on board *SDO*). It is therefore possible to establish a complete database of limb prominences. Second, the high time resolution of the data allows us to track their evolution, even small changes. Third, the projection effect can be minimized for certain parameters, such as height and radial speed. Fourth, they are complementary to the catalogs of on-disk filaments. Further, so far there is no well-established online catalog for limb prominences.

2. METHOD

Our system consists of five modules. The first module is to select prominence candidates; the second one is to extract necessary parameters for further usage; the third one is to discriminate prominences from other non-prominence features, such as active regions and noise; the fourth one is to track the prominences for the evolution; and the last one is to generate a catalog of prominences with final parameters. Here we use EUVI 304 Å data from *STEREO-B*/SECCHI to illustrate these processes.

2.1. Module 1: Prominence Candidate Selection

The functions of module 1 are illustrated in Figure 1. A raw EUVI 304 Å image is shown in Figure 1(a). The background brightness above the limb generally decreases with increasing distance, r, from the solar center. Similarly, the prominences near the solar surface are much brighter than those at high altitude (for example, comparing prominence A and B marked in the image). The variation of the brightness of the prominence with r is further discussed in Section 4.3. Although region B is too dark to be noticed in the raw image, we still consider it a prominence candidate for its higher density compared to the ambient coronal plasmas.

The first step of processing is to use a technique similar to the normalizing-radial-graded filter (Morgan et al. 2006) to rescale the brightness so that the contrast is independent of r. To do this, a background image is first created, which is a circular symmetric image with respect to the center of the solar disk as shown in Figure 1(b). The pixel value at any r is just the average value of all the pixels along the circle at r in the original image. It is obvious that the brightness of background plasma does drop quickly as r increases. Then, we obtain the rescaled image (Figure 1(c)) by using the following formula:

$$\text{Rescaled Image} = \frac{\text{Original Image (Figure 1(a))} + \delta}{\text{Background Image (Figure 1(b))} + \delta}. \quad (1)$$

Here, δ is a small value to avoid dividing by a near-zero value. Both prominence material A and B become much clearer. For the *STEREO-B*/EUVI 304 Å images, δ is chosen to be 5 through

trial and error; however, this number may change for other instruments, depending on the signal-to-noise ratio.

Further recognition, which applies the technique of region-growing with certain thresholds, is based on the rescaled image. The following process is similar to those by, e.g., Gao et al. (2002) and Bernasconi et al. (2005), and thus we just briefly describe it here. First, we set a threshold th_{knl} to pick all the pixels with larger values as kernels. The searching region is from 1 $R_{\odot}$ to r_{max1}, where r_{max1} is an upper boundary, above which there is no kernel selected. The boundary of r_{max1} is needed because the signal-to-noise ratio will become low when approaching the edge of the telescope's field of view. For *STEREO-B*/SECCHI EUVI images, we choose the value of 1.7 $R_{\odot}$. The selected kernels serve as the seeds, from which the whole prominence regions grow out. Figure 1(d) is a binary image showing the kernels. Here some small kernels, which are isolated pixels due to the presence of noise, have been removed by applying a morphological *opening* operator with a box size of $s_n \times s_n$. Second, we let these kernels grow by setting another smaller threshold th_{pro}, i.e., all neighboring pixels with values larger than th_{pro} will be included in the growing regions. For the cases where several regions are close to each other but not connected, we use a morphological *closing* operator with a box size of $s_m \times s_m$ to merge them together. Some regions, whose areas are smaller than th_{area}, are discarded to further prevent noise-like features from being included. The resultant regions are the candidate prominences as shown in Figure 1(e). Figure 1(f) is obtained by superimposing the boundaries of the recognized regions on the rescaled image. The set of arguments discussed above is listed in Table 1.

2.2. Module 2: Parameter Extraction

Once we have the boundary of a region of interest, the extraction of parameters of the region is straightforward. According to the scaling information in the header of the FITS file of the image, we can calculate the area (A) and average brightness (F) of the region, the minimum and maximum positions in both radial and azimuthal directions (r_{bot}, r_{top}, θ_{min}, and θ_{max}), and the centroid of brightness (r_{cen} and θ_{cen}). It should be noted that as the signal-to-noise ratio decreases significantly near the edge of the field of view, we set another upper boundary r_{max2}, slightly larger than r_{max1}, and consider that the parameters of any prominence extending into the region above it might be unreliable.

Further, we linearize (i.e., get the spine of) the region to obtain certain morphological information. Figure 2 presents a sample. We use the morphological *thin* operator (refer to, e.g., Lam et al. 1992) to get the skeleton (panel b) of the prominence of interest (panel a). Usually, a skeleton is too intricate because of the many branches involved. To remove trivial branches, we first calculate the length (weighted by the rescaled brightness) of each branch. Then, for branches connecting to the same node, we compare their lengths and save the largest one. The above steps are iterated until there are only two ends (panel c). The resultant curve is further smoothed to get the spine (panel d) by applying the two-dimensional mean filter method. One should note that any region of interest will be finally simplified to a line with only two ends even if it actually has three or more ends/footpoints.

Since most prominences have a loop-like structure in morphology, we keep the length of the spine as the characteristic length (L) of the recognized region. Meanwhile, the obtained spine can be used in three-dimensional reconstruction of a prominence if it is viewed in two different visual angles at
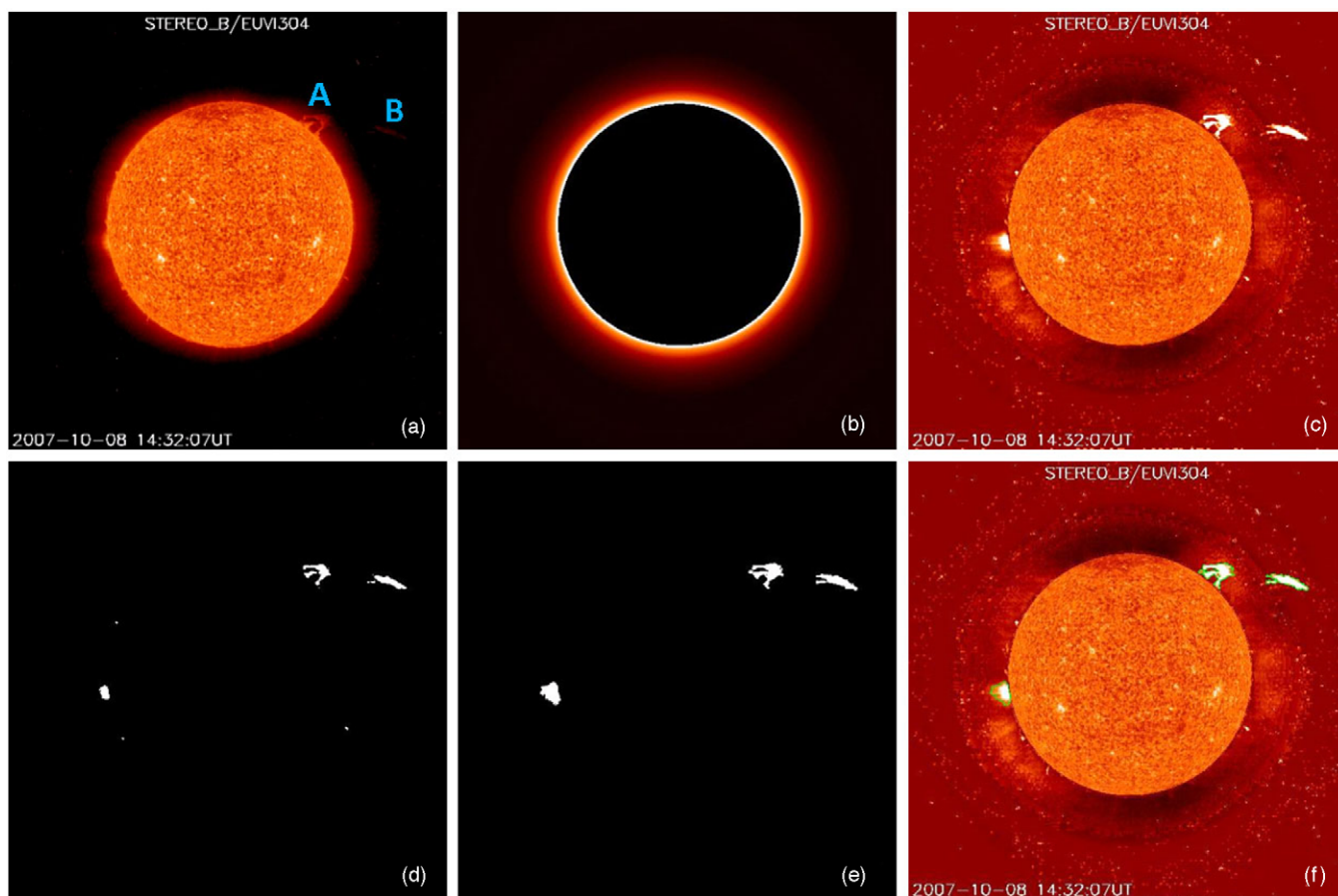
Figure 1. Sample image from 2007 October 8 illustrating the processes of selecting prominence candidates. (a) The raw EUVI 304 Å image, (b) circular symmetrical background image, (c) rescaled image, (d) binary image of selected kernels, (e) binary image of possible prominence regions, and (f) the rescaled image with the boundaries of the recognized regions. The bright patch above the east limb in (f) is an active region, which will be removed by module 3.

Table 1
List of the Arguments Used by SLIPCAT for *STEREO-B*/EUVI 304 Å Data

Arguments	Values	Units	Interpretation
δ[a]	5.0		A small value used in creating rescaled images (see Section 2.1)
th_{knl}[a]	2.0		A threshold for kernel selection (see Section 2.1)
th_{pro}[a]	1.7		A threshold for region growing (see Section 2.1)
r_{max1}[b]	1.7	$R_\odot$	An upper boundary in r, above which there is no selected kernel (see Section 2.1)
r_{max2}[b]	1.73	$R_\odot$	An upper boundary in r. The parameters of any prominence extending into the region above it is considered to be unreliable (see Section 2.2)
s_n[c]	5	pixels	Define a box used to remove noise-like kernels (see Section 2.1)
s_m[c]	5	pixels	Define a box used to merge regions that are very close to each other (see Section 2.1)
th_{area}	500	Mm^2	A threshold to remove very small regions (see Section 2.1)
th_{dis}	2	hr	A threshold to judge if a prominence has disappeared (see Section 2.4)

Notes.
[a] Pixel values in rescaled images, probably changing for different instruments.
[b] Depending on the range of field of view and the signal-to-noise ratio.
[c] Need to be changed for different spatial resolution of images.

the same time (e.g., by the *STEREO* twins or combined with *SOHO*), which will be studied specifically in another paper.

2.3. Module 3: Non-prominence Feature Removal

While photons in EUV 304 Å images mainly come from He II emissions, they also have contaminations from hot coronal lines (e.g., Zhang et al. 1999). As a result, prominences are not the only bright feature in EUV 304 Å wavelength, and active regions also appear bright. In the work by Foullon & Verwichte (2006), the authors realized this fact and used observations in other wavelengths to exclude active regions from

their detected bright regions. The regions recognized through our first two modules also contain active regions and some noisy features. We do not, however, try to involve other observations in our detection, which will make the system more intricate and prone to additional errors. In our system, the previously extracted parameters for each recognized region will be used to discriminate real prominences from these non-prominence features, as discussed below.

Prominences have a different appearance from other features. For example, in morphology, a prominence usually looks like a loop or stick, while an active region is shaped like a round blob.
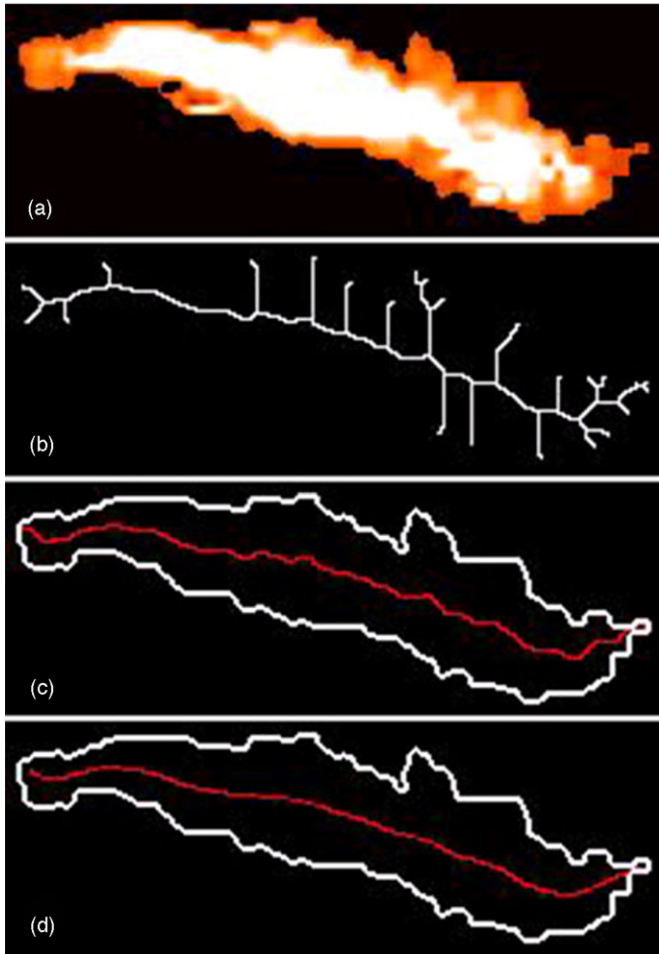
Figure 2. Extracting the spine of a prominence: (a) original region, (b) skeleton, (c) spine, and (d) smoothed spine.
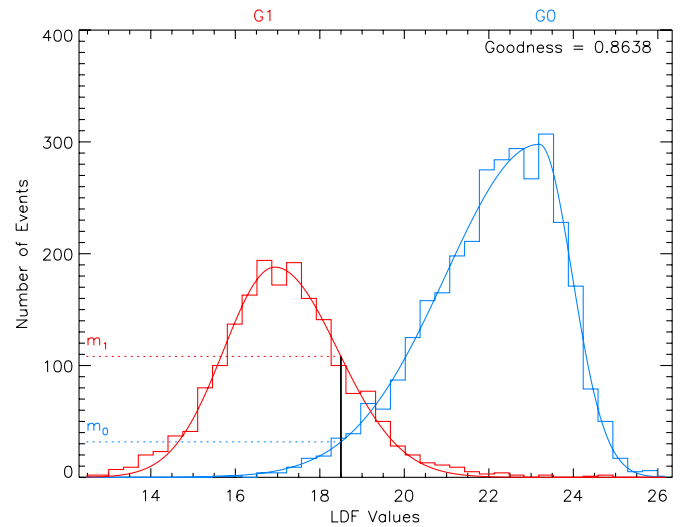
In brightness, a prominence is almost flat over radial distance in the rescaled image, while an active region is not. Thus, one can use a classification method to remove the non-prominence features. There are many classification methods, e.g., linear discriminant analysis (LDA), support vector machines (SVM), and neural networks (NN; see Meyer et al. 2003). The method we adopted here is the LDA. One can refer to the paper by, e.g., Fisher (1936) for the principle of the LDA.

Through many tests, the parameters $\ln A$ (standing for the size of a region), $\ln \frac{A}{L}$ (for the shape), and $\ln \chi_F^2$ (for the variation in brightness, where χ_F^2 is the value of Chi-square goodness-of-fit statistic for the brightness F as a linear function of distance r) are chosen to construct the linear discriminant function (LDF). Our sample contains 5066 regions from a total of 3780 images (4 images per day, near 00:00, 06:00, 12:00, and 18:00 UT, respectively, from 2007 April 1 to 2009 October 31). Each region is checked by eye to determine which group it belongs to, the prominences or non-prominences. On the basis of this large collection of features of known classification, or the truth table, we derive the LDF as

$$X = 1.460 \ln A + 1.103 \ln \frac{A}{L} - 0.491 \ln \chi_F^2 \qquad (2)$$

or

$$X = 14.20 \frac{\ln A}{\langle \ln A \rangle} + 4.70 \frac{\ln \frac{A}{L}}{\langle \ln \frac{A}{L} \rangle} + 1.36 \frac{\ln \chi_F^2}{\langle \ln \chi_F^2 \rangle}, \qquad (3)$$

Figure 3. Result of the LDA of the truth table. The two groups, prominences (labeled G1) and non-prominence features (G0), are indicated in red and blue colors, respectively.

where the quantity $\langle f \rangle$, the mean value of f calculated based on our truth table, is used to normalize the parameters so that we can learn the importance of the parameters from their factors. The area A is the most important to discriminate a prominence from other features because it has the largest factor 14.20. However, it should be noted that some very big prominences might be missed due to the important role of area in the discrimination (for example, the erupting prominence on 2009 November 2). But such misses usually take place in several frames, and therefore will not significantly affect the tracking result of the whole evolution process of the prominences identified in other frames.

Figure 3 shows the discriminant result. It can be seen that the group of prominences (labeled G1) generally has different LDF values from the group of non-prominence features (G0). Since there is still an overlap between the two groups, we evaluate the goodness of LDF by

$$G = 1 - \frac{n_o}{n}, \qquad (4)$$

where n_o is the number of regions whose LDF value falls within the overlap and n is the total number of regions in the truth table. In other words, the value of G is the ratio of the area of non-overlapped regions to the sum of the areas occupied by the two groups in Figure 3. $G = 1$ means the LDF can completely discriminate between the two groups. In our case, the goodness is about 0.86.

Based on Equation (2), we can calculate the LDF value of any recognized region, and compare it with the derived distribution of the LDF values, which is fitted with Gaussian distribution functions as shown by the curves in Figure 3, to determine how likely it is that the region is a prominence. The likelihood of a region being a prominence is given by

$$P = \frac{m_1}{m_0 + m_1}, \qquad (5)$$

where m_0 and m_1 are the values of the fitted Gaussian distribution functions corresponding to the LDF value for groups 0 and 1, respectively. A region with $P \leqslant 50\%$ is treated as a non-prominence feature and is therefore discarded.
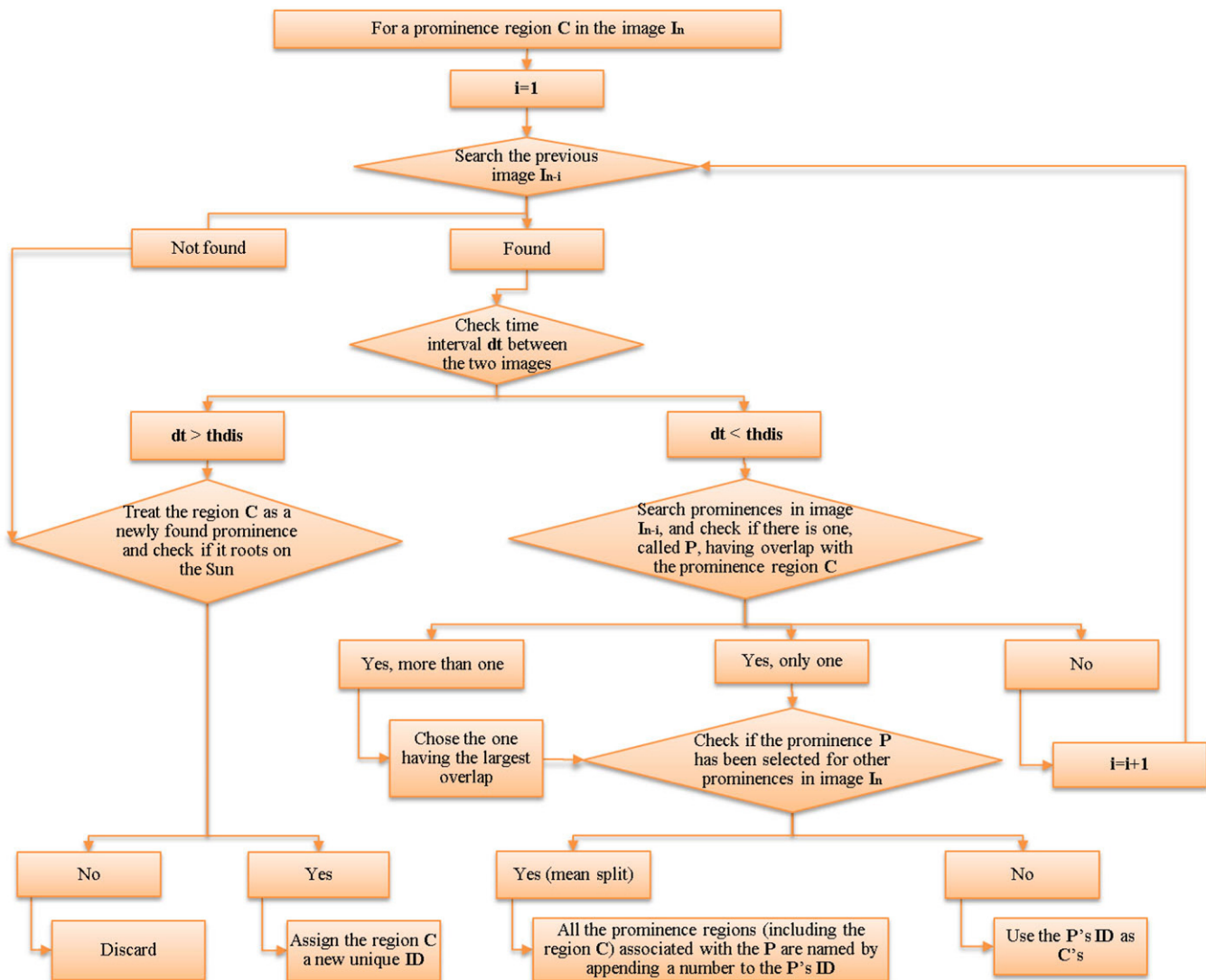
Figure 4. Flow chart illustrating the prominence tracking process.
(A color version of this figure is available in the online journal.)

### 2.4. Module 4: Prominence Tracking

Our method to track the evolution of a prominence is quite simple. Figure 4 is the flow chart showing how we track a prominence. The top of the flow chart is a prominence to be tracked in an image, and the bottom of the chart gives the four possible results. Since the flow chart is detailed enough, we will not repeat it here. There are only several things that we would like to point out.

First, the criterion used to judge if a prominence region is evolved from a prominence region in the previous image is to check whether or not there is an overlap between them in spatial domain. This requires that the cadence of the data should be high enough, especially when studying a fast erupting prominence. According to our statistical result (see Figure 5), which is plotted based on our catalog (refer to Section 2.5), most prominences move with a speed of about 4 km s^{-1} or less in the radial or azimuthal direction, few ones may reach up to more than 100 km s^{-1}. Considering that their characteristic length is $L \approx 60$ Mm, it is inferred that a cadence of 4 hr (for 4 km s^{-1} speed, or a cadence of 15 minutes for 100 km s^{-1}) is basically sufficient for prominence tracking, which is much slower than the 10 minute cadence of *STEREO*/SECCHI EUVI 304 Å data.

Second, we use a time threshold th$_{dis}$ to determine whether or not a prominence has disappeared, i.e., if a previously named prominence has not been found in the successive images for a duration of th$_{dis}$, it is treated as having disappeared. A previously detected prominence may temporarily and intermittently "disappear." Such a "disappearing" may not be real; it may be a result of the unstable quality or jittering of images (although we have done some treatments on the original data as mentioned in Section 2.1) and/or small changes in the prominence itself, which cause the brightness of the prominence to temporarily decrease to below the threshold th$_{knl}$ or even th$_{pro}$. Note that this situation only happens to some small and/or faint prominences, not to major ones. Setting a relatively long time duration th$_{dis}$ can efficiently track the entire evolution process of a prominence. Here we let th$_{dis} = 2$ hr.

Third, in our tracking process, the case that a prominence splits into two or more parts is considered (see the third result in the flow chart). However, we do not deal with the case of merging, which means there is more than one prominence region (for example, A and B) in the previous image merging together
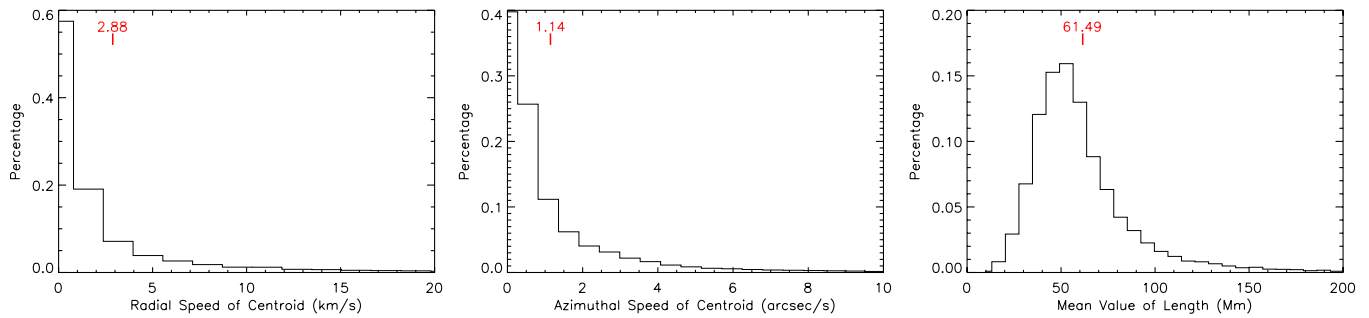
Figure 5. Histograms of the radial (left panel) and azimuthal speed (middle panel) of the centroid of prominences and the characteristic length (right panel). The average values are marked in the plots. The upper limits of the *x*-axes are chosen to make the plots readable, but do not mean the maximum values (the same treatment applies to Figures 6 and 7).

(A color version of this figure is available in the online journal.)

and associated with only one prominence region (say C) in the current image. The merging of prominences is ambiguous, as the phenomenon can also be interpreted as the prominence region A (or B) disappearing and region B (or A) evolving to region C. In this scenario, no region merging takes place.

Fourth, if a prominence is identified as a new one (see the left side of the flow chart), we will check if it connects to the solar surface. Only those rooted on the Sun are considered real prominences. This justification is based on the assumption that no newly emerged prominence is disconnected from the Sun.

2.5. Module 5: Catalog Generation

Solar prominences above the limb are identified and tracked by the above four modules. All the input arguments to SLIPCAT for the *STEREO-B*/SECCHI EUVI 304 Å data are summarized in Table 1, and the primary parameters extracted for each prominence at a certain time are summarized in Table 2. Since we have the parameters of each prominence in its time sequence, it becomes possible to automatically extract its kinetic evolution information. For example, we can derive the velocity $\mathbf{v}_c$ and acceleration $\mathbf{a}_c$ of the centroid, from the variations of r_{cen} and θ_{cen} with time. Also we can get some peak and average values of the above parameters, such as $A_{\max}$, A_{ave}, etc. Moreover, for each prominence, we give the confidence level by the following formula:

$$C = \begin{cases} 1, & \overline{P} > 90\% \\ 2, & 75\% < \overline{P} \leqslant 90\% \\ 3, & 50\% < \overline{P} \leqslant 75\%, \end{cases} \quad (6)$$

where $\overline{P}$ is the average value of the likelihood of the prominence over its period of tracking. A resultant online catalog is established at http://space.ustc.edu.cn/dreams/slipcat/, where one can find all the final output parameters. The analyses in the following sections are based on the parameters in the catalog.

We note that it is straightforward to apply the system to other spacecraft data, e.g., *SDO*/AIA data (which is in our planning), though we present here only *STEREO-B* data. The only part we need to modify is the input arguments listed in Table 1. Besides, the code is written in IDL language, and modules 1–3 and modules 4 and 5 can run separately. Modules 1–3 have nothing to do with the causal relationship among the images, thus they can process images serially or in parallel. Using a computer with 2.33 GHz Intel Xeon CPUs, 3 GB memory, and a Linux operating system, it takes 36 s on average for modules 1–3 to process one full-size EUVI image and takes only 0.29 s for modules 4 and 5. Thus, to process the sequence of images

Table 2
List of the Primary Parameters Extracted for Each
Prominence at a Certain Time

Parameter	Interpretation
$(r_{\mathrm{cen}}, \theta_{\mathrm{cen}})$	Coordinates of the centroid of the brightness
$r_{\mathrm{bot}}, r_{\mathrm{top}}$	Give the span of a prominence in the radial direction
$\theta_{\min}, \theta_{\max}$	Give the span of a prominence in the angular direction
A	Area of a prominence in units of Mm^2
L	Characteristic length of a prominence in units of Mm
F	Average brightness recorded in the original image
P	Likelihood of a recognized region to be a prominence

over one day with the cadence of 10 minutes, it needs about 1.45 hr. The *SDO*/AIA data have higher resolution (4096×4096 pixels) and faster cadence (10 s), which will require modules 1–3 to spend much more time. It is estimated that it will take about 347 hr if we serially process such one-day images in the machine mentioned above. Thus, to reduce the processing time to less than 24 hr, a small cluster with 15 or more CPUs is needed to run modules 1–3 in parallel, which should be affordable.

3. PERFORMANCE AND LIMITATIONS

SLIPCAT detected 19,140 prominences from the *STEREO-B* data during the beginning of 2007 April to the end of 2009 October. Figure 6 shows the distributions of the duration of the prominences and the number of frames in which a prominence is detected. It is found that 6348 prominences (33%) are detected in only one frame (upper panels), and the rest exhibit a roughly linear correlation between the duration and frame number as shown in the lower panel of Figure 6. The solid line in the scatter plot marks the expected relationship between the duration and frame number for the imaging cadence of 10 minutes. A point above the line means that the instrument operates in a higher-cadence mode and the prominence is well tracked, while a point below the line implies that the prominence is missing in some frames. Most points distribute around the solid line. We define a prominence as poorly tracked when it matches one of the following two criteria: (1) it is detected in only one frame and (2) it is missing in 2/3 or more of the expected frames (marked by the dashed line in the scatter plot). Note that the radial speeds of prominences are no more than 160 km s^{-1} (see Figure 5), which implies a prominence is expected in at least five or more frames. Thus, a prominence detected in only two frames is also treated as poorly tracked. There are a total of 9663 (50.5%) poorly tracked prominences during the period of interest. As to the rest, we call them well-tracked prominences.
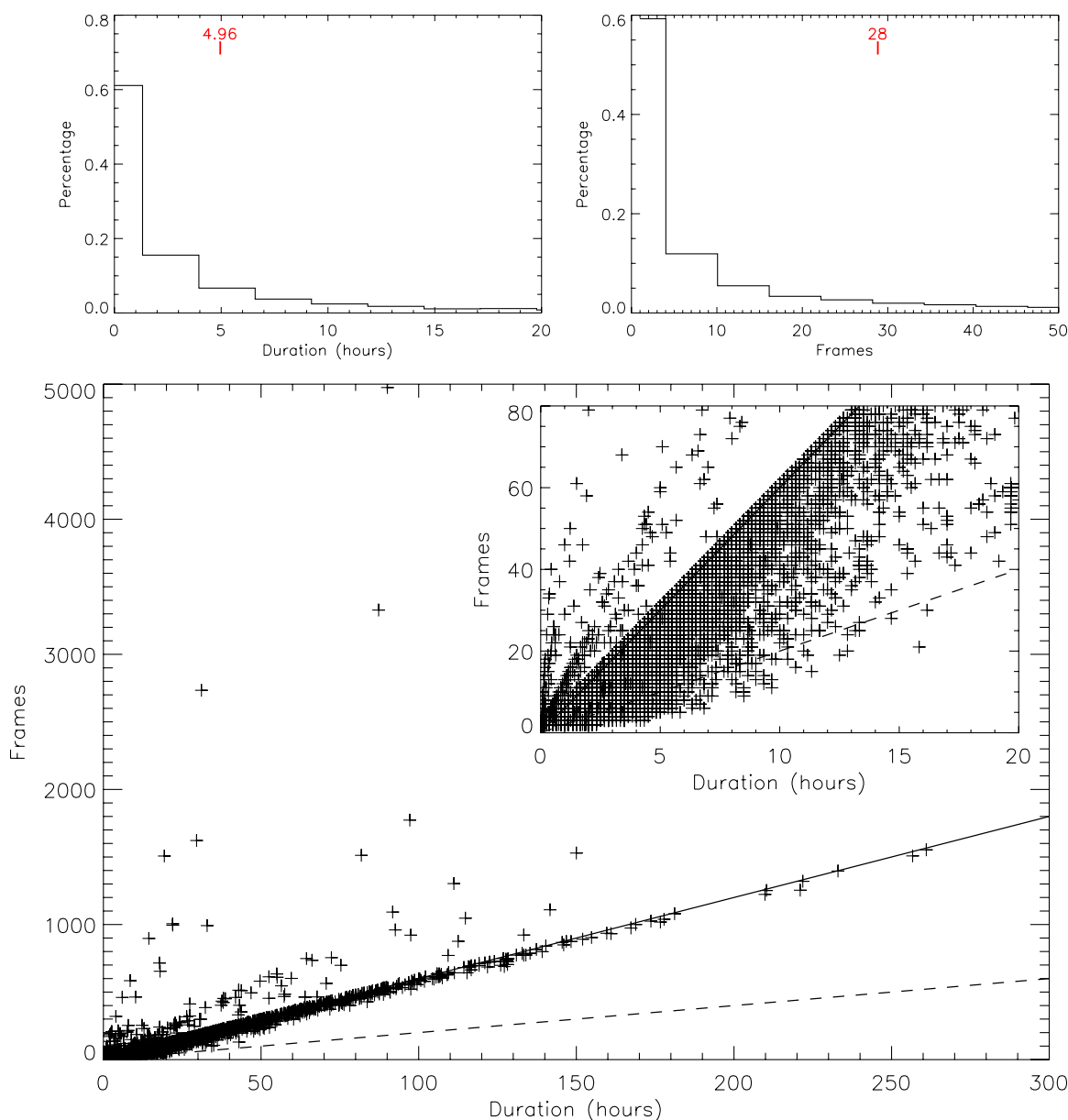
Figure 6. Upper panels: histograms of the duration and the number of frames. The average values are marked in the plots. Lower panel: relationship between the duration and frames. The solid line indicates the expected relationship at a cadence of 10 minutes.
(A color version of this figure is available in the online journal.)

These poorly tracked prominences are generally small and their top portions (or leading edges) lie low. These are revealed in Figure 7. The average value of maximum areas of poorly tracked prominences is 976 Mm^2, about three times smaller than that of well-tracked ones; the average value of maximum lengths of poorly tracked prominences is about 60 Mm, nearly half of that of well-tracked ones; and the average top position of poorly tracked prominences is about 21 Mm lower than that of well-tracked ones. As early as in 1932, Pettit (1932) had concluded that prominences are usually about 60 Mm long or more, 10 Mm thick, and 50 Mm high. These numbers are close to what we obtained here using modern data. By checking movies in the catalog, we find that the causes of such poorly tracked prominences are probably a result of the features being marginal (close to the detection thresholds), contamination of nearby non-prominence features, and of course, the limitation of the detection algorithm. The parameters of these prominences may

not be extracted correctly, and therefore they will be excluded from our statistical analysis in Section 4.

The upper left panel of Figure 6 suggests that some prominences may appear for up to 260 hr, which seems too long to be possible. Due to the solar rotation, in theory a prominence at a height of about 56 Mm (the average value of top position) above the equator can stay visible for no more than 80 hr. With increasing latitude, this lasting duration may increase. If the prominence extends along the longitudinal direction, the lasting duration can be even longer. Figure 8 shows that the prominences with long duration generally appear at high latitude, where quiescent or polar crown prominences are usually present. Thus, it is possible to have such long-duration prominences.

Figure 9 shows the daily counts of the well-tracked prominences. For most days, about 14 prominences are detected. However, in extreme cases, there may be as many as 32 or as few as zero prominences a day. By checking the Hα images from Big
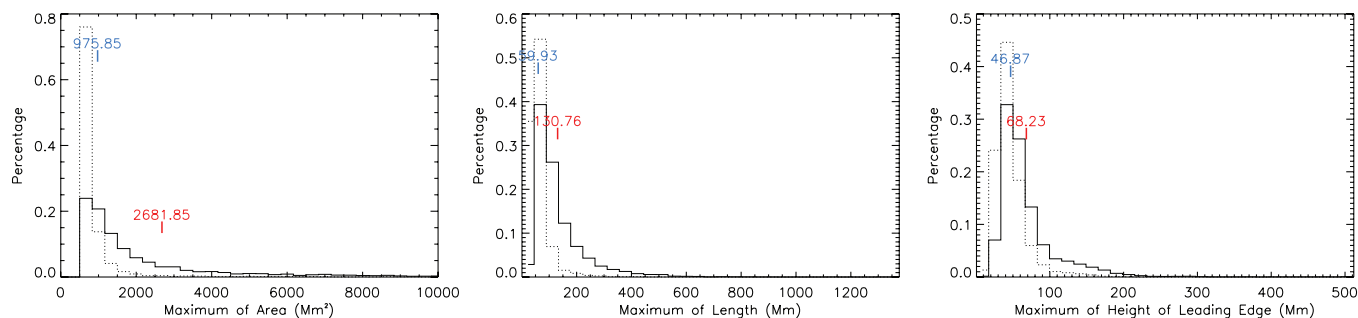
Figure 7. Histograms of the maximum area (left panel), characteristic length (middle panel), and top position (right panel) for the well-tracked (solid line) and poorly tracked (dotted line) prominences. The average values (red for well-tracked and blue for poorly tracked) are marked in the plots.

(A color version of this figure is available in the online journal.)
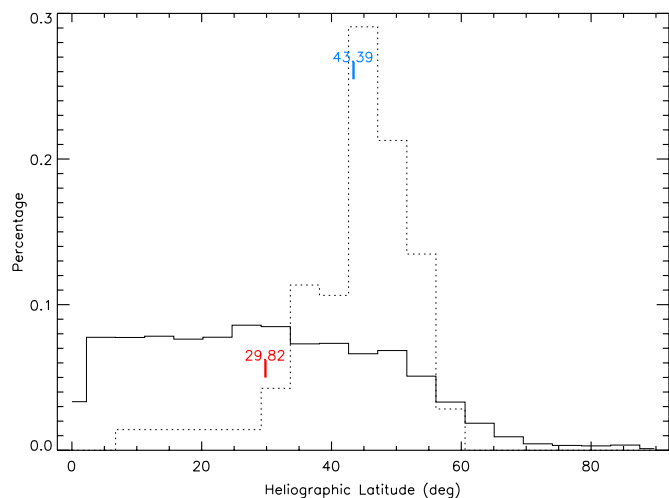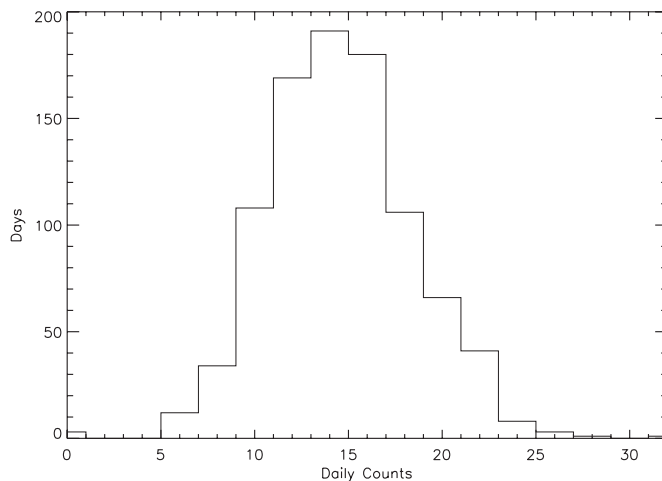

Figure 8. Histograms of the latitude for long-duration ($\geqslant$80 hr, dotted line) and short-duration (<80 hr, solid line) prominences, respectively. The average values (red for short duration and blue for long duration) are marked in the plots.

(A color version of this figure is available in the online journal.)

Figure 9. Distribution of daily counts of limb prominences.

Bear Solar Observatory (BBSO), it is found that there are more filaments during solar maximum than solar minimum. During 2007–2009, the extreme solar minimum, there are usually only a few filaments in an Hα image, that is inconsistent with our results. To make sure that the prominences identified by SLIP-CAT are not non-prominence features, we compare the EUVI 304 Å images with the Hα image as shown in Figure 10. The date of these images is 2009 October 7, which is arbitrarily chosen; on this day, the *STEREO-B* spacecraft was 58° behind the Earth. Thus, the west limb in the *STEREO-B*/EUVI 304 Å image corresponds to about 33° west of the central meridian in the Hα image. One can find that the western hemisphere in the Hα image is largely free of features except for three prominences standing at high latitude (as denoted by arrows). Actually, there is also a prominence at a low latitude, which can be clearly seen in the EUVI images (marked by a circle). The comparison demonstrates that there are probably some small prominences visible in EUV 304 Å emission line, but invisible in Hα. It is also supported by many observational facts that solar filaments are generally more extended in EUV lines than in Hα (e.g., Heinzel et al. 2001). Thus, it can be concluded that SLIPCAT is sensitive to recognizing prominences, even those invisible in Hα.

Further, the accuracy of the parameters listed in the catalog should be addressed. First of all, it should be noted that the values

of these parameters just give us the information of prominences during the period when they are detected, not necessarily through their whole lifetime. Second, some parameters suffer from the projection effect, e.g., the value of area depending on the angle of view. Third, some parameters, e.g., velocity, change rates of area, and brightness, are automatically derived from fitting data points. Thus, their accuracy depends on the number of frames, the fitting function, and the complexity of the prominence. As an example, Figure 11 presents an erupting prominence observed on 2008 November 13. This prominence rose from the southeast limb, and partially erupted. During its eruption, the prominence splits into three major parts (see Figure 11(d)): one escaped from the Sun, one remained on the Sun, and the other erupted but returned back to the Sun later. SLIPCAT tracks the entire eruption process. The left panel of Figure 12 displays the height–time profile of the leading edge of the prominence. The solid line is a quadratic fit through the data points and the dashed line is a linear fit. Due to the splitting of the prominence, the fitting curves obviously do not reflect the reality. The correct treatment is to study the evolution of the split parts separately. The right panel shows the height–time profile of the escaping part. However, the fitting result for that part is still not satisfactory enough. The time at about 11:00 UT is a critical point, before which the escaping part was slowly rising, while after which it experienced a fast acceleration and erupted quickly. Thus, a two-stage linear fitting is more appropriate than a pure linear or quadratic fitting. However, we still choose linear and quadratic functions to fit all the detected prominences, because this treatment can be easily implemented
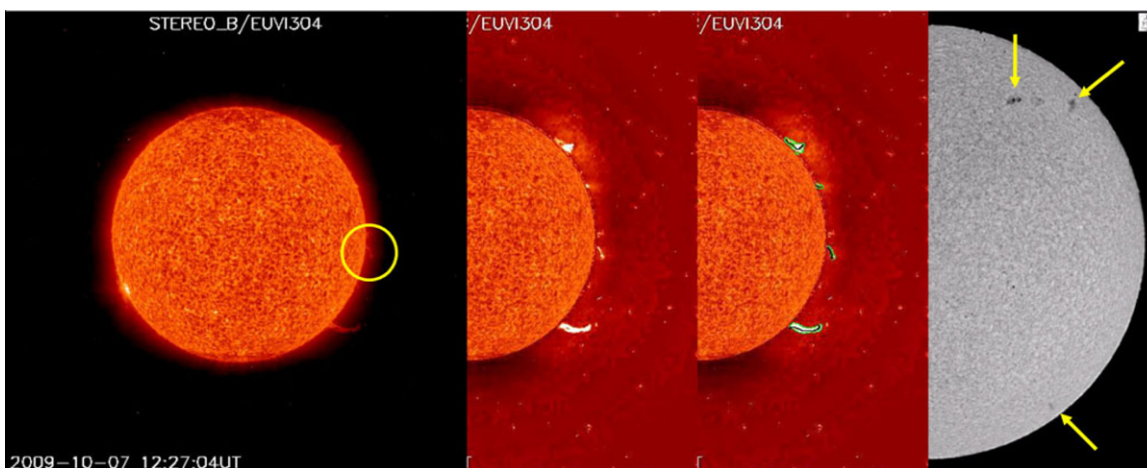
Figure 10. Comparison of the EUV 304 Å prominences viewed by *STEREO* with Hα filaments viewed from the Earth. From left to right, they are original EUV 304 Å image, rescaled image, rescaled image with selected prominences, and Hα image from BBSO.
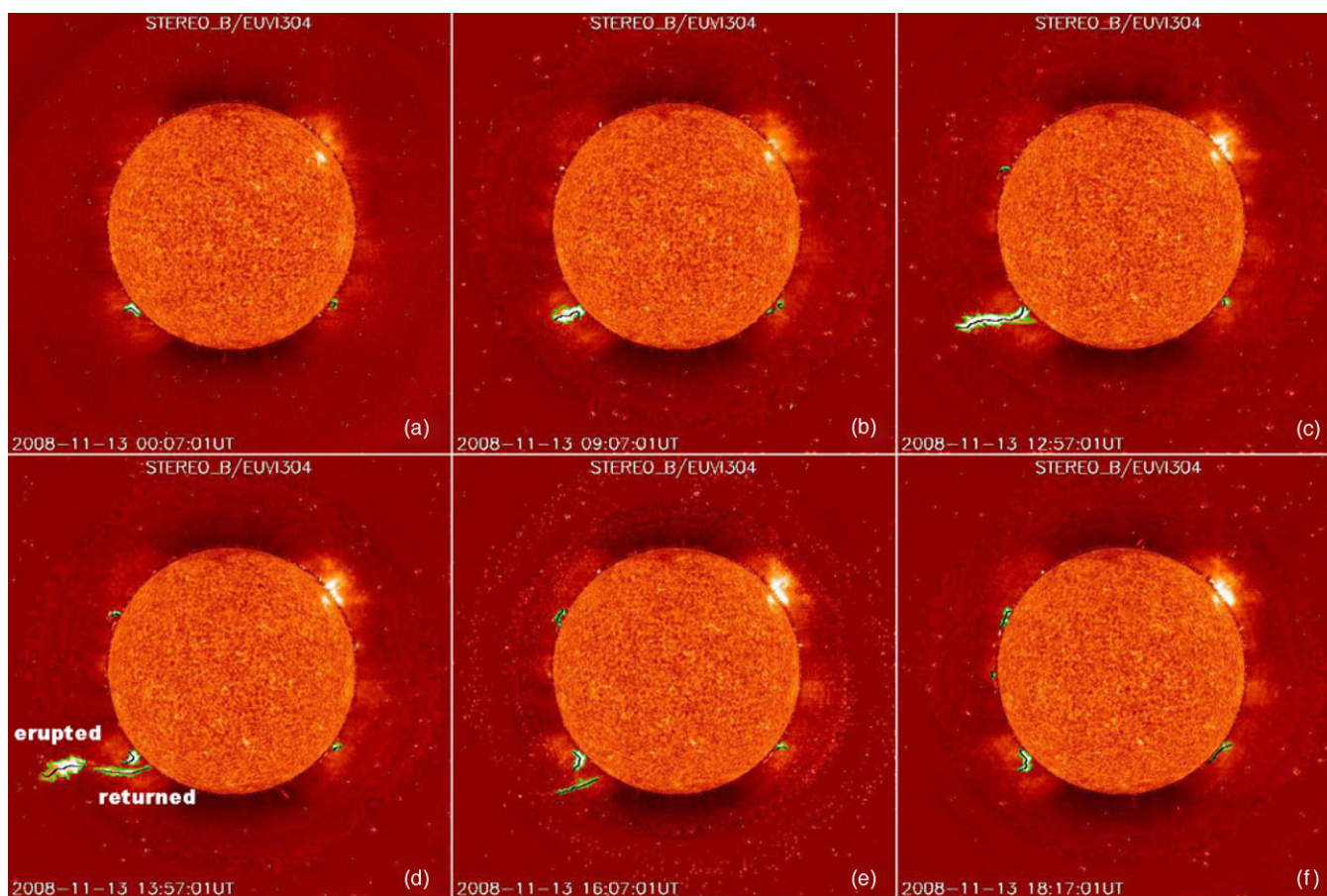

Figure 11. Erupting prominence on 2008 November 13, which splits into three parts during the eruption. One escaped from the Sun, one remained on the Sun, and the other erupted but returned back to the Sun.

in an automated way. One should keep in mind that the fitting results only give a coarse estimation of the average speed (or change rates of area and brightness) and acceleration.

4. PRELIMINARY STATISTICAL RESULTS

Now SLIPCAT has a complete data set for *STEREO-B* data. A catalog of prominences seen from *STEREO-A* will be generated soon. Here we would like to present some statistical results of the *STEREO-B* prominences. Since we probably do

not get very accurate parameters for prominences as discussed in the last section, the results obtained here are just preliminary. However, from a statistical point of view, these results should be significant. In the following analysis, all the poorly tracked prominences are removed. Such prominences are generally extremely small and stay at low altitude as discussed in Section 3, thus the statistical results might suffer from the bias of selection; one should treat it as a statistics of moderate and major prominences. Moreover, we will include prominences with all confidence levels. There are only 257 (2.7%) prominences with
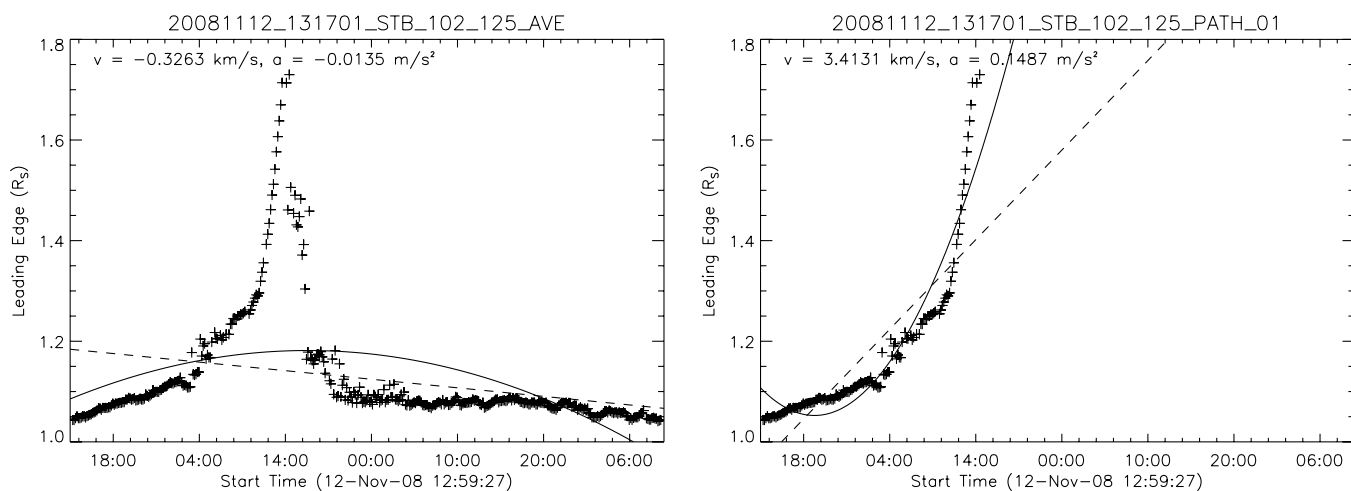
Figure 12. Height–time profiles of the leading edge of the prominence presented in Figure 11. The left panel is for the whole prominence system, while the right panel is for the escaping part only. The solid line is a quadratic fit through the data points and the dashed line is a linear fit.
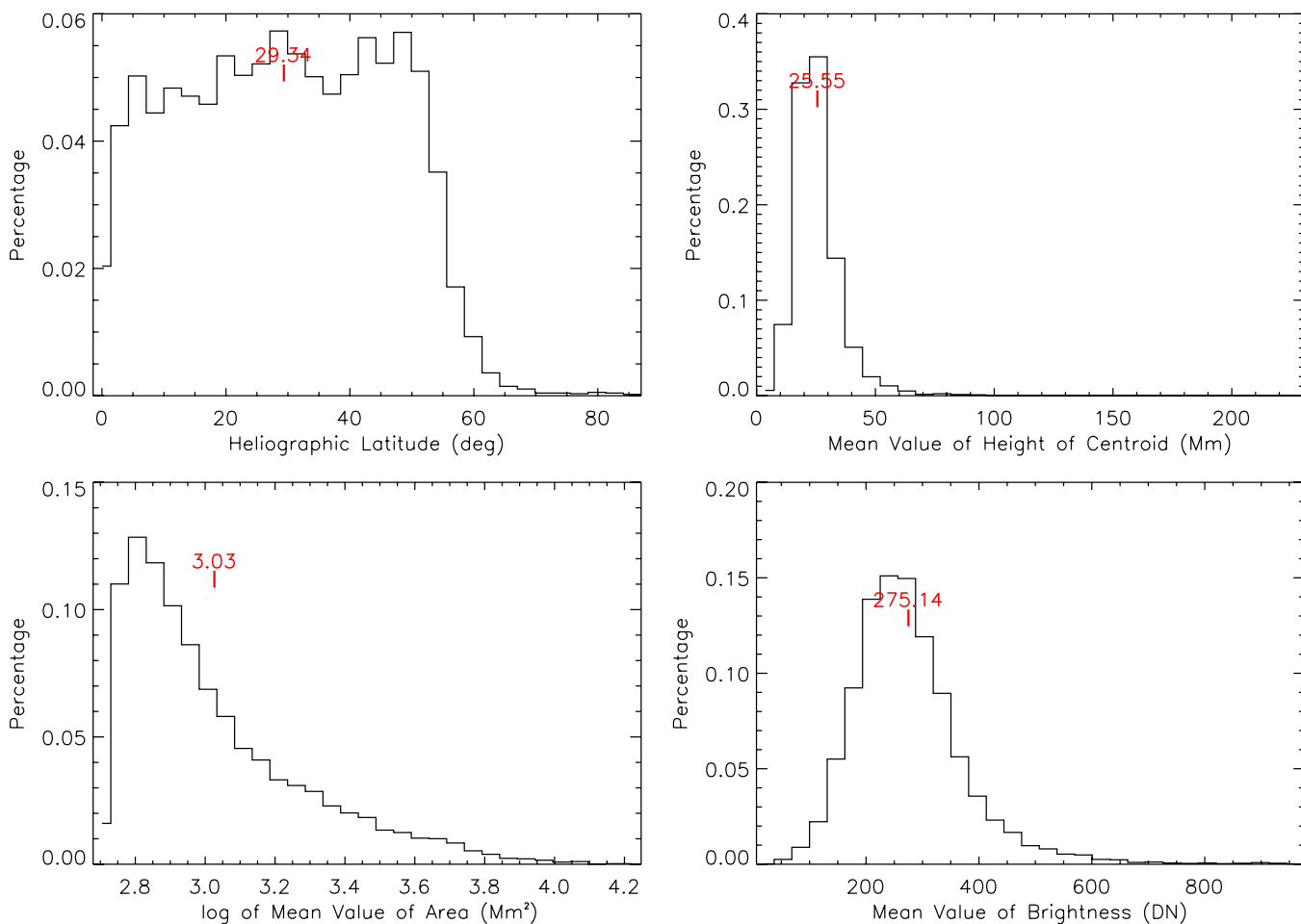
Figure 13. Histograms of static parameters: (upper left panel) heliographic latitude at the first appearance, mean values of (upper right panel) height of centroid, (lower left panel) area and (lower right panel) brightness. The average values of these distribution are marked in the plots.

(A color version of this figure is available in the online journal.)

confidence levels of 2 or 3, which represents a rather small fraction in the database.

4.1. Static Parameters

First of all, static parameters of the 9477 well-tracked prominences are investigated. These parameters are (1) the

heliographic latitude of the centroid of a prominence at the first detection, (2) the mean value of the height of the centroid, (3) the mean value of the area, and (4) the mean value of the brightness of a prominence. The distribution of heliographic latitudes (folded at equator) shown in the upper left panel of Figure 13 suggests that 99% prominences appear below 60°. One may suspect that the lower count at high latitude may be
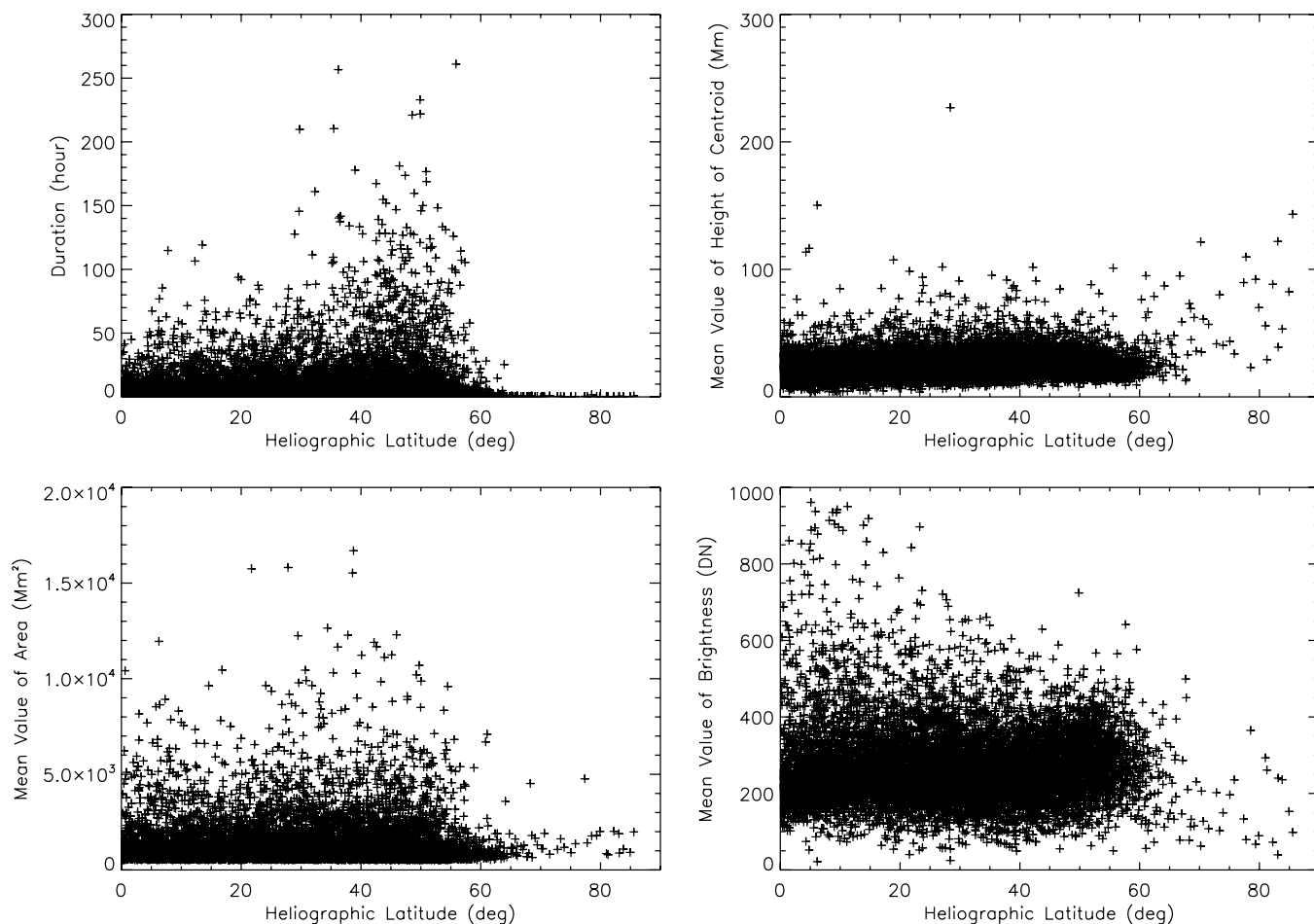
Figure 14. Correlations of heliographic latitude with (upper left panel) duration, mean values of (upper right panel) the height of centroid, (lower left panel) area, and (lower right) brightness.

caused by the perception that a prominence at high latitude is usually quiescent or a polar crown prominence and generally is long lived and extended. However, the scatter plot of the latitude versus duration in the upper left panel of Figure 14 indicates that this perception is wrong, as it clearly shows that the durations of the prominences above 60° are short. The long-duration prominences appear around 30°–60°, which probably implies that long extended prominences arise there. Similar result can also be found in Figure 8 though there we include the poorly tracked prominences. Moreover, from rescaled EUV 304 Å images, one can clearly find that the regions above 60° are generally occupied by polar coronal holes. By checking the catalog and movies, we find that the detected "prominences" above 60° are usually polar jets. Since their number is small, the statistical results obtained below will not be affected by including these "false" prominences.

The distribution of the heights of centroids suggests that about 82% of prominences stay at around 26 Mm above the solar surface. There is no obvious dependence of the height on the latitude as shown by the scatter plot in Figure 14. The previous statistical study by Ananthakrishnan (1961) suggested that the heights of prominences vary between 15 and 150 Mm. Pettit (1932) gave a value of about 50 Mm, and Kim et al. (1988) showed that there is a peak at about 28 Mm in the distribution of heights. Theoretical work suggests that the height of a prominence depends on the gradient of ambient coronal magnetic field strength with height (e.g., Filippov & Den 2000). Our result is consistent with these studies.

The area and brightness can be usually used to evaluate if a prominence is a major one or not. Similarly, we use the mean values of them to show the distribution. The average projected area on the plane of sky of all prominences is about 1072 Mm^2. Nearly 60% prominences have an area smaller than the average value. Figure 14 suggests that the area is unrelated with the latitude. The brightness is recorded as digital number (DN) by the CCD camera. Its distribution is close to a Gaussian one, with an average value at around 275 DN. It can be as low as 20 DN or as high as 960 DN. The scatter plot in Figure 14 shows a weak dependence of the brightness on the latitude. The low-latitude prominences may reach to a higher brightness than middle- to high-latitude prominences.

4.2. Dynamic Parameters

For dynamic properties, we investigate the velocities (both radial and azimuthal) and change rates of area and the brightness of prominences. Here we use the leading edge rather than the centroid in the analysis of the radial speed. One may also use the radial speed of the centroid, but it will bring a large error in the case that a prominence splits into two parts: one erupting and the other staying on the Sun. The histograms in Figure 15 show the radial and azimuthal speeds. A speed of 10 arcsec s^{-1} corresponds to about 33 km s^{-1} at the solar surface. More than 80% of prominences have no obvious motion in either the radial or the azimuthal direction, and the value of zero is the most probable speed (as shown in the insets). A few prominences may move upward at about more than 100 km s^{-1}, and also there are
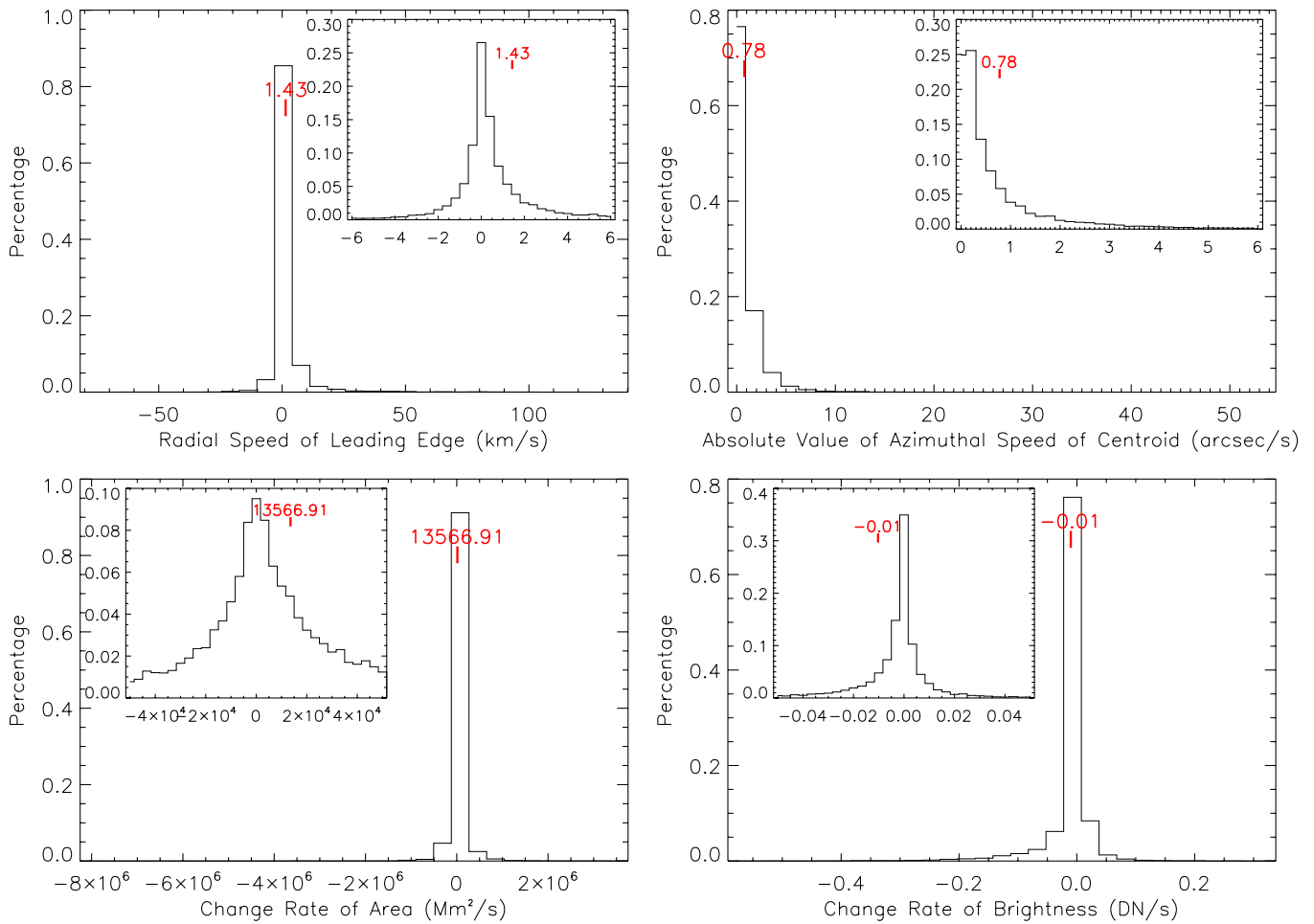
Figure 15. Histograms of dynamic parameters: (upper left panel) radial speed of leading edge, (upper right panel) azimuthal speed of centroid, (lower left panel) change rate of area, and (lower right panel) brightness. The averaged values are marked in the plots.

(A color version of this figure is available in the online journal.)

37 ($\approx 0.4\%$) prominences having a radial speed < -20 km s^{-1} or an azimuthal speed > 10 arcsec s^{-1}. The former could be easily understood that an erupting prominence may have a large outward speed, but the cause is not obvious for the latter.

In Section 3 we have mentioned that the quality or precision of the fitting results largely depends on the number of measurements. More measurements can efficiently reduce errors, and therefore the fitting results will be more reliable. By checking the movies of the 37 prominences with unusual speed, we find that 34 prominences are detected in no more than 6 frames, and the speeds of most (not all) of these 34 prominences are not correctly reflected by the fitting. However, since we have a large sample in the statistics, such a small fraction of corrupted events will not distort the overall picture shown in Figure 15. On the other hand, it is also realized that there are indeed some prominences having a large downward or azimuthal speed. The large downward speed may either present a real motion or is just resulted from the shrinking of the prominence. Any further analyses on such extreme events will be pursued in the future.

Similarly, for most prominences the change rates of area and brightness are quite small although the average value of the change rate of area is about 1.35×10^4 Mm^2 s^{-1}. There are 106 (1.1%) prominences with an absolute value of change rate of area $> 10^6$ Mm^2 s^{-1} or brightness > 0.25 DN s^{-1}. The movies reveal that some prominences do change this fast.
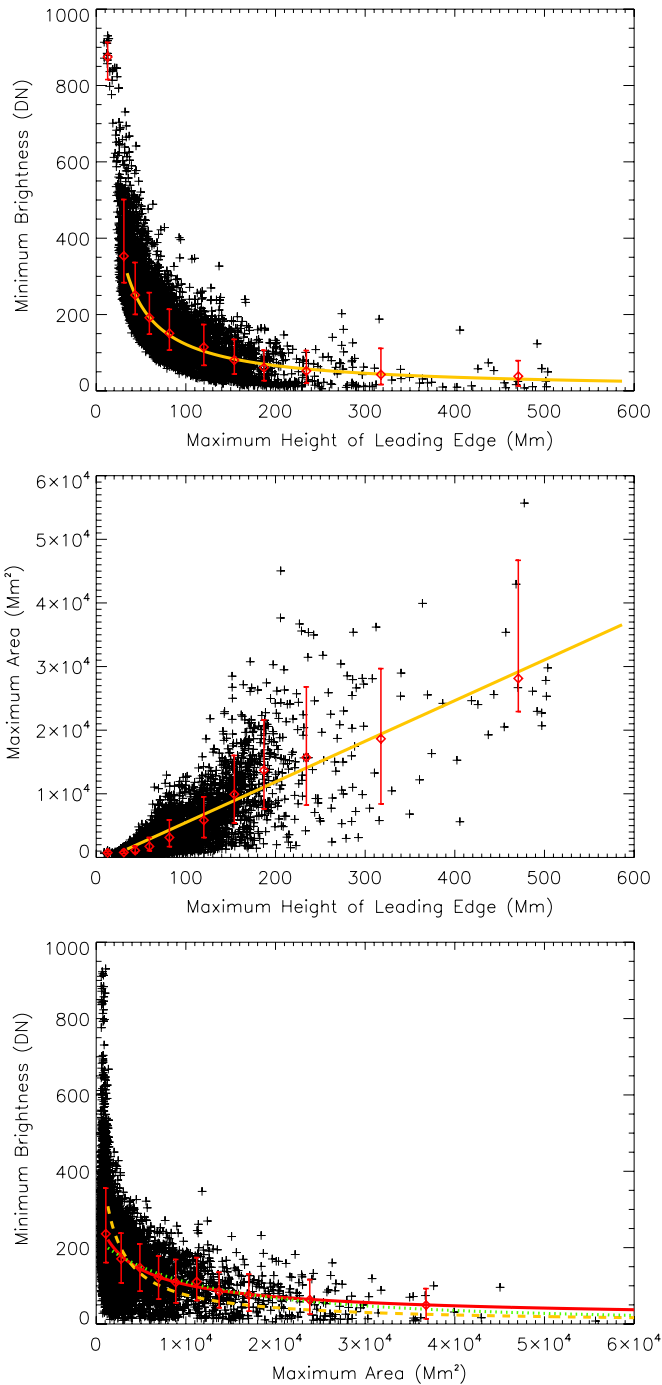
4.3. Fading of Prominences

It is well known that prominences generally become dimmer as they rise. The reason could be the heating of prominence materials (e.g., Mouradian & Martres 1986; Ofman et al. 1998; Hanaoka & Shinkawa 1999), mass loss (e.g., Rusin & Rybansky 1982), and/or expansion (e.g., Bemporad 2009). The first one is a thermal process, and the other two are dynamic processes (e.g., Mouradian & Martres 1986; Mouradian et al. 1995; Tandberg-Hanssen 1995). Here we will look into this issue in a statistical way. In our parameters, we have the information of altitude, brightness, and area of prominences, and have no direct information about the heating or mass of prominences. Thus, it is impossible to make a comprehensive study of the causes of the prominence fading, but we can learn how significant the factor of the expansion is.

The first panel in Figure 16 shows a strong anti-correlation between the brightness and the height of prominences. The higher altitude makes the prominence dimmer. The diamond symbols with error bars indicate the average values of brightness around certain altitude. These points are fitted to obtain the following empirical formula:

$$F = 7.47 \times 10^3 (h + 1.29)^{-0.891} \text{ DN}, \quad (7)$$

where $h \geqslant 35$ Mm is the height from solar surface in units of Mm. It describes the dependence of the brightness on the

Figure 16. Scatter plots between minimum brightness, maximum area, and maximum height of the leading edge.

the expansion of prominences must be a cause of the prominence fading when they are rising or erupting.

Combining the two equations, we derive the relationship between the brightness and area (indicated by the dashed line in the last panel of Figure 16):

$$F = 3.04 \times 10^5 (A + 9.88 \times 10^2)^{-0.891} \text{ DN}, \qquad (9)$$

where A is in the units of Mm^2. Also we can directly fit the data in the last panel that leads to

$$F = 3.96 \times 10^4 (A + 2.42 \times 10^3)^{-0.631} \text{ DN} \qquad (10)$$

as shown by the solid line. Approximately, area is proportional to $V^{2/3}$, where V is the volume of a prominence. If there is no mass loss or gain, the density of a prominence ρ is inversely proportional to the volume, i.e., $\rho \propto V^{-1} \propto A^{-1.5}$. The brightness can be a proxy of the density of the plasma in the temperature window corresponding to EUV 304 Å emission line. If there is no heating or cooling, the function $F = c_0(A + c_1)^{-1.5}$ is supposed to describe the relationship between the brightness and area. By fitting the data points, we obtain the dotted line given by

$$F = 4.76 \times 10^8 (A + 1.66 \times 10^4)^{-1.5} \text{ DN}. \qquad (11)$$

It is found that the solid and dashed lines are close to the dotted one, which implies that, in a statistical point of view, the expansion is probably one of the major causes of the fading of prominences during their rise or eruption. Of course, this statistical conclusion could not be true for all individual cases. As revealed by, e.g., Ofman et al. (1998) and Hanaoka & Shinkawa (1999), the heating process may play an important role in the disappearances of some prominences.

5. SUMMARY

We have developed an automated system of catching and tracking solar limb prominences in EUV 304 Å images. The system, called SLIPCAT, is able to generate (1) a catalog of solar limb prominences and (2) some characteristic parameters of each detected prominence, including the height, position angle, area, length, brightness, and their first and second derivatives with respect to time. SLIPCAT is composed of five modules: (1) prominence candidate selection, (2) parameter extraction, (3) non-prominence feature removal, (4) prominence tracking, and (5) catalog generation. At present, an online catalog for *STEREO-B*/EUVI 304 Å data has been generated (refer to http://space.ustc.edu.cn/dreams/slipcat/), and catalogs for *STEREO-A*/SECCHI/EUVI and *SDO*/AIA data are in preparation.

Based on the *STEREO-B*/EUVI 304 Å data, SLIPCAT proved to perform well in detecting limb prominences.

1. It can distinguish real prominences from non-prominence features, e.g., active regions, without observations in other wavelengths by using the technique of LDA. The goodness of the overall classification is at about an 86% success rate.
2. It detected as many as 9477 well-tracked prominences during 2007 April–2009 October, which means on average about 10 events per day. Compared to Hα data, it is found that SLIPCAT is sensitive enough to recognize almost all prominences, even those invisible in Hα images or very small ones.

altitude. The points below 35 Mm are excluded in the fitting as they seem to follow another pattern.

The second panel exhibits an evident positive linear correlation between the area and height. It means a prominence at a higher altitude tends to be larger. This phenomenon supports the picture that when a prominence rises or erupts, it expands as well. The expansion is probably caused by the weaker constraint of ambient atmosphere at a higher altitude. Similarly, we fit the data points marked by the diamond symbols, and get

$$A = 64h - 906 \, \text{Mm}^2. \qquad (8)$$

The reversed correlations of Equations (7) and (8) suggest that

3. Thanks to the high-cadence EUV 304 Å data, SLIPCAT is able to quantitatively provide the detailed evolution processes of prominences without manual interventions. The upper right panel of Figure 6 implies that at least a well-tracked prominence is detected in 28 images on average; and the case in Figure 12 shows that such high-cadence detection allows us to make a detailed analysis of its evolution, including its eruption, oscillation, etc.

However, not all the parameters extracted by SLIPCAT can precisely reveal the real behavior of prominences. The limitations have been addressed in the last paragraph of Section 3. Summarized here, they are that (1) the parameters characterize the properties of prominences during the period they are detected, not over the whole lifetime, (2) they suffer from the projection effect, and (3) the speeds and change rates of area, length, and brightness, which are derived from linear and quadratic fittings, may not be accurate.

By applying SLIPCAT to the *STEREO-B*/EUVI 304 Å data from 2007 April to 2009 October, we obtain the following preliminary statistical results of solar limb prominences.

1. On average, there are about 10 prominences standing above the solar limb per day during the solar minimum. For most days, about 14 prominences are expected to be detected, and sometimes the number could be as large as 32 or as small as zero.
2. Most (99%) prominences appear below the latitude of $60°$, and the long extended prominences tend to arise between the latitudes of $30°$ and $60°$.
3. Most (82%) prominences have a height of about 26 Mm from the solar surface.
4. The projected area of a prominence on the plane-of-sky is about 1072 Mm^2 on average, and nearly 60% of prominences have a smaller area.
5. Most prominences are quite stable during the period they are detected; no obvious change in position, area, or brightness can be found.
6. Particularly, more than 80% of prominences do not show obvious motion in either the radial or the azimuthal direction. However, some prominences have an upward speed of more than 100 km s^{-1}, and a few prominences present a significant downward or azimuthal speed.
7. The brightness of prominences is anti-correlated with the height. The prominences at higher altitude look dimmer.
8. The area of prominences is positively correlated with the height. The prominences at higher altitude are generally larger.
9. From a statistical point of view, the expansion of prominences is probably one of the major causes of the fading of prominences during their rise or eruption.

REFERENCES

Ananthakrishnan, R. 1961, ApJ, 133, 969
Bemporad, A. 2009, ApJ, 701, 298
Bernasconi, P. N., Rust, D. M., & Hakim, D. 2005, Sol. Phys., 228, 97
Chiuderi Drago, F., Alissandrakis, C. E., Bastian, T., Bocchialini, K., & Harrison, R. A. 2001, Sol. Phys., 199, 115
Delaboudiniere, J.-P., et al. 1995, Sol. Phys., 162, 291
Engvold, O., & Brynildsen, N. 1986, in NASA Conf. Publ. 2442, Temperatures of Quiescent Prominences Measured from Hydrogen Paschen and Ca ii IR lines, ed. A. I. Poland (Washington, DC: NASA), 97
Filippov, B. P., & Den, O. G. 2000, Astron. Lett., 26, 322
Fisher, R. A. 1936, Ann. Eugenics, 7, 179
Foullon, C., & Verwichte, E. 2006, Sol. Phys., 234, 135
Fuller, N., Aboudarham, J., & Bentley, R. D. 2005, Sol. Phys., 227, 61
Gao, J., Wang, H., & Zhou, M. 2002, Sol. Phys., 205, 93
Gilbert, H. R., Holzer, T. E., Burkepile, J. T., & Hundhausen, A. J. 2000, ApJ, 537, 503
Gopalswamy, N., Shimojo, M., Lu, W., Yashiro, S., Shibasaki, K., & Howard, R. A. 2003, ApJ, 586, 562
Hanaoka, Y., & Shinkawa, T. 1999, ApJ, 510, 466
Hanaoka, Y., et al. 1994, PASJ, 46, 205
Heinzel, P., Schmieder, B., & Tziotziou, K. 2001, ApJ, 561, L223
Hiei, E., Ishiguro, M., Kosugi, T., & Shibasaki, K. 1986, in NASA Conf. Publ. 2442, Dark Filaments Observed at 8.3 mm and 3.1 mm, in Coronal and Prominence Plasmas, ed. A. I. Poland (Washington, DC: NASA), 109
Hirayama, T. 1986, in NASA Conf. Publ. 2442, The Density and Thickness of Quiescent Prominences, in Coronal and Prominence Plasmas, ed. A. I. Poland (Washington, DC: NASA), 149
Kim, I. S., Klepikov, V. Y., Koutchmy, S., Stepanov, A. I., & Stellmacher, G. 1988, Soln. Dannye Byull., 1988/1, 75
Labrosse, N., Dalla, S., & Marshall, S. 2010, Sol. Phys., 262, 449
Labrosse, N., & Gouttebroze, P. 2001, A&A, 380, 323
Lam, L., Lee, S. W., & Suen, C. Y. 1992, IEEE Trans. Pattern Anal. Mach. Intell., 14, 869
Madjarska, M. S., Vial, J.-C., Bocchialini, K., & Dermendjiev, V. N. 1999, in ESA-SP 446, 8th *SOHO* Workshop, Plasma Dynamics and Diagnostics in the Solar Transition Region and Corona, ed. J.-C. Vial & B. Kaldeich-Schümann (Paris: ESA), 467
Martin, S. F. 1998, Sol. Phys., 182, 107
Meyer, D., Leisch, F., & Hornik, K. 2003, Neurocomputing, 55, 169
Morgan, H., Habbal, S. R., & Woo, R. 2006, Sol. Phys., 236, 263
Mouradian, Z., & Martres, M. J. 1986, in NASA Conf. Publ. 2442, The Heating of Filaments as a Disappearance Process, in Coronal and Prominence Plasmas, ed. A. I. Poland (Washington, DC: NASA), 221
Mouradian, Z., Soru-Escaut, I., & Pojoga, S. 1995, Sol. Phys., 158, 269
Ofman, L., Kucera, T. A., Mouradian, Z., & Poland, A. I. 1998, Sol. Phys., 183, 97
Patsourakos, S., & Vial, J.-C. 2002, A&A, 385, 1073
Penn, M. J., Arnaud, J., Mickey, D. L., & Labonte, B. J. 1994, ApJ, 436, 368
Pettit, E. 1932, ApJ, 76, 9
Poland, A. I., ed. 1986, NASA Conf. Publ. 2442, Coronal and Prominence Plasmas: Proceedings of Workshops Held at Goddard Space Flight Center, 1985 April 9–11, 1986 April 8–10 (Washington, DC: NASA)
Rusin, V., & Rybansky, M. 1982, BAICz, 33, 219
Schmahl, E. J., Foukal, P. V., Noyes, R. W., Reeves, E. M., Timothy, J. G., Vernazza, J. E., Withbroe, G. L., & Huber, M. C. 1974, Sol. Phys., 39, 337
Shih, F. Y., & Kowalski, A. J. 2003, Sol. Phys., 218, 99
Tandberg-Hanssen, E. 1995, The Nature of Solar Prominences (Dordrecht: Kluwer)
Zhang, J., White, S. M., & Kundu, M. R. 1999, ApJ, 527, 977
Zharkova, V. V., Aboudarham, J., Zharkov, S., Ipson, S. S., Benkhalil, A. K., & Fuller, N. 2005, Sol. Phys., 228, 361